



HATS-71b: A Giant Planet Transiting an M3 Dwarf Star in TESS Sector 1

G. Á. Bakos^{1,23,27}, D. Bayliss², J. Bento³, W. Bhatti¹, R. Brahm^{4,5,6}, Z. Csabry¹, N. Espinoza^{7,25,26}, J. D. Hartman¹, Th. Henning⁷, A. Jordán^{5,6}, L. Mancini^{7,8,9}, K. Penev¹⁰, M. Rabus^{5,7,24}, P. Sarkis⁷, V. Suc⁵, M. de Val-Borro¹¹, G. Zhou¹², R. P. Butler¹³, J. Crane¹⁴, S. Durkan¹⁵, S. Shectman¹⁴, J. Kim¹, J. Lázár¹⁶, I. Papp¹⁶, P. Sári¹⁶, G. Ricker¹⁷, R. Vanderspek¹⁷, D. W. Latham¹², S. Seager¹⁷, J. N. Winn¹, J. Jenkins¹⁸, A. D. Chacon¹⁹, G. Fűrész¹⁷, B. Goeke¹⁷, J. Li¹⁸, S. Quinn¹², E. V. Quintana²⁰, P. Tenenbaum¹⁸, J. Teske¹⁴, M. Vezie¹⁷, L. Yu¹⁷, C. Stockdale²¹, P. Evans²², and H. M. Relles¹⁴

¹Department of Astrophysical Sciences, Princeton University, Princeton, NJ 08544, USA

²Department of Physics, University of Warwick, Coventry CV4 7AL, UK

³Research School of Astronomy and Astrophysics, Australian National University, Canberra, ACT 2611, Australia; gbakos@astro.princeton.edu

⁴Center of Astro-Engineering UC, Pontificia Universidad Católica de Chile, Av. Vicuña Mackenna 4860, 7820436 Macul, Santiago, Chile

⁵Instituto de Astrofísica, Pontificia Universidad Católica de Chile, Av. Vicuña Mackenna 4860, 7820436 Macul, Santiago, Chile

⁶Millennium Institute of Astrophysics, Av. Vicuña Mackenna 4860, 7820436 Macul, Santiago, Chile

⁷Max Planck Institute for Astronomy, Königstuhl 17, D-69117 Heidelberg, Germany

⁸Department of Physics, University of Rome Tor Vergata, Via della Ricerca Scientifica 1, I-00133 Roma, Italy

⁹INAF—Astrophysical Observatory of Turin, Via Osservatorio 20, I-10025 Pino Torinese, Italy

¹⁰Department of Physics, University of Texas at Dallas, Richardson, TX 75080, USA

¹¹Astrochemistry Laboratory, NASA Goddard Space Flight Center, 8800 Greenbelt Road, Greenbelt, MD 20771, USA

¹²Harvard-Smithsonian Center for Astrophysics, 60 Garden Street, Cambridge, MA 02138, USA

¹³Department of Terrestrial Magnetism, Carnegie Institution for Science, Washington, DC 20015, USA

¹⁴The Observatories of the Carnegie Institution for Science, 813 Santa Barbara Street, Pasadena, CA 91101, USA

¹⁵Astrophysics Research Centre, Queens University, Belfast, UK

¹⁶Hungarian Astronomical Association, 1451 Budapest, Hungary

¹⁷Massachusetts Institute of Technology, Cambridge, MA, USA

¹⁸SETI Institute/NASA Ames Research Center, Mountain View, CA, USA

¹⁹Millennium Engineering and Integration Co./NASA Ames Research Center, Arlington, VA, USA

²⁰NASA Goddard Space Flight Center, Greenbelt, MD, USA

²¹Hazelwood Observatory, Victoria, Australia

²²El Sauce Observatory, Río Hurtado, Coquimbo, Chile

Received 2018 December 5; revised 2020 March 17; accepted 2020 March 31; published 2020 May 18

Abstract

We report the discovery of HATS-71b, a transiting gas giant planet on a $P = 3.7955$ day orbit around a $G = 15.35$ mag M3 dwarf star. HATS-71 is the coolest M dwarf star known to host a hot Jupiter. The loss of light during transits is 4.7%, more than in any other confirmed transiting planet system. The planet was identified as a candidate by the ground-based HATSouth transit survey. It was confirmed using ground-based photometry, spectroscopy, and imaging, as well as space-based photometry from the NASA Transiting Exoplanet Survey Satellite mission (TIC 234523599). Combining all of these data, and utilizing Gaia DR2, we find that the planet has a radius of $1.024 \pm 0.018 R_J$ and mass of $0.37 \pm 0.24 M_J$ (95% confidence upper limit of $<0.80 M_J$), while the star has a mass of $0.4861 \pm 0.0060 M_\odot$ and a radius of $0.4783 \pm 0.0060 R_\odot$.

Unified Astronomy Thesaurus concepts: Exoplanets (498); Exoplanet detection methods (489); Transit photometry (1709); Radial velocity (1332); Astronomical instrumentation (799); Observational astronomy (1145)

Supporting material: machine-readable tables

1. Introduction

Much has been learned about the physical properties of exoplanets in the nearly three decades following the discovery of the exoplanet candidate HD 114762b (Latham et al. 1989). As of 2018 September 27, the NASA Exoplanet Archive lists 3791 confirmed and validated exoplanets²⁸ the majority of which were found by the NASA *Kepler* mission via the transit method.

Among the confirmed planets are 418 short-period gas giant planets ($P < 10$ days, and $M_p > 0.2 M_J$ or $R_p > 0.7 R_J$). These are the so-called hot Jupiters. Especially important are those 375 hot Jupiters that are known to *transit* their host stars. These objects are among the best-studied planets, providing a wealth of information about their physical properties. To illustrate their importance, among the 270 planets for which the mass and radius have both been determined with a precision of 20% or better, 235 are hot Jupiters. Of the 133 planets for which the (sky-projected) stellar obliquity has been measured, 117 are hot Jupiters (TEPCat; Southworth 2011). Similarly, the majority of exoplanets with observational constraints on the properties of their atmospheres are hot Jupiters (e.g., Madhusudhan 2018). All of these observations have been greatly facilitated by the frequently occurring and deep ($\sim 1\%$) transits presented by these systems.

All but 12 of the 418 hot Jupiters in the NASA Exoplanet Archive have been found around F, G, or K-type host stars

²³ MTA Distinguished Guest Fellow, Konkoly Observatory, Hungary.

²⁴ Visiting astronomer, Cerro Tololo Inter-American Observatory, National Optical Astronomy Observatory.

²⁵ Bernoulli Fellow.

²⁶ IAU-Gruber Fellow.

²⁷ Packard Fellow.

²⁸ Objects with $M < 30 M_J$ are included in this catalog of confirmed exoplanets, though those objects with $M > 13 M_J$ are often referred to as brown dwarfs rather than exoplanets.

($4000 \text{ K} < T_{\text{eff}} < 7300 \text{ K}$, or $0.6 M_{\odot} < M < 1.6 M_{\odot}$ if T_{eff} is not given in the database). One of the hot Jupiters in this sample is around a B star, seven are around A stars, and only four have been found around M dwarf stars. The hot Jupiters that have previously been discovered around M dwarf stars include:

1. Kepler-45 b ($M_{\text{p}} = 0.505 \pm 0.090 M_{\text{J}}$, $M_{\text{S}} = 0.59 \pm 0.06 M_{\odot}$, $T_{\text{eff}} = 3820 \pm 90 \text{ K}$; Johnson et al. 2012),
2. HATS-6 b ($M_{\text{p}} = 0.319 \pm 0.070 M_{\text{J}}$, $M_{\text{S}} = 0.574^{+0.020}_{-0.027} M_{\odot}$, $T_{\text{eff}} = 3724 \pm 18 \text{ K}$; Hartman et al. 2015),
3. NGTS-1 b ($M_{\text{p}} = 0.812^{+0.066}_{-0.075} M_{\text{J}}$, $M_{\text{S}} = 0.617^{+0.023}_{-0.062} M_{\odot}$, $T_{\text{eff}} = 3916^{+71}_{-63} \text{ K}$; Bayliss et al. 2018),
4. HD 41004 B b ($M_{\text{p}} \sin i = 18.37 \pm 0.22 M_{\text{J}}$, $M_{\text{S}} \sim 0.4 M_{\odot}$; Zucker et al. 2003).

The last of these was detected in the radial velocity (RV) observations of the M2V component of a K1V+M2V visual binary, and the inferred $19 M_{\text{J}}$ mass of the brown-dwarf companion is a lower limit. The other three objects are transiting systems.

Theoretical models of planet formation and evolution have predicted that hot Jupiters should be less common around M dwarf stars than around solar-type stars (Mordasini et al. 2012). While there is some observational support for this prediction from RV surveys (Johnson et al. 2010), the number of M dwarfs that have been systematically surveyed for hot Jupiters is still too low to be certain of this conclusion (Obermeier et al. 2016).

One of the main goals in current exoplanet research is to expand the sample of well-characterized hot Jupiters known around M dwarfs and A or earlier-type stars. This will allow the occurrence rate of hot Jupiters to be measured as a function of stellar mass, and will also enable the dependence of other properties of planetary systems on stellar mass to be studied. Some of these properties that might be investigated include the orbital obliquities of the planets, the degree of inflation in the their radii, and their atmospheric properties.

Giant planets transiting M dwarf stars also provide at least two observational advantages over planets of similar size transiting larger stars. They produce very deep transits. In principle, a giant planet could completely obscure a very low-mass star, although no such system has been discovered to date. The deep transits allow for observations with a higher signal-to-noise ratio (S/N), especially if conducted in the infrared (IR), where the stars have a higher photon flux density. The stars themselves undergo very little evolution over the lifetime of the Galaxy, allowing a more precise constraint on the mass and radius of the star (and hence of the planet) from the available observations compared to what can be done for more massive stars (e.g., Hartman et al. 2015).

The primary challenge in discovering transiting hot Jupiters around M dwarfs is the faintness of these stars. In order to survey a sufficient number of M dwarfs to detect the rare cases of transiting hot Jupiters, it is necessary to observe stars down to $V \sim 15$ mag, which is fainter than the limits of many of the ground-based transit surveys that have been productive at discovering transiting hot Jupiters. The two ground-based surveys that have discovered transiting hot Jupiters around M dwarfs are the HATSouth survey (Bakos et al. 2013) and the NGTS survey (Wheatley et al. 2018). Both of these projects use larger aperture telescopes than the other wide-field transit

surveys (0.18 m in the case of HATSouth and 0.20 m in the case of NGTS) allowing for greater sensitivity to M dwarf stars.

In this paper we present the discovery of HATS-71b by the HATSouth survey, the fifth hot Jupiter found around an M dwarf star, and the fourth transiting system of this type. With an effective temperature of $\sim 3400 \text{ K}$, and a spectral type of M3V, HATS-71 is the coolest M dwarf known to host a transiting hot Jupiter. The 4.7% deep transits are also the deepest of any transiting system discovered to date. The planet was first detected by HATSouth, and then confirmed using ground-based spectroscopic and photometric follow-up. It was also recently observed in Sector 1 of the NASA Transiting Exoplanet Survey Satellite mission (TESS, Ricker et al. 2015), and included in the first set of alerts released to the public. In this paper we present all of these data and analyze them to determine the physical properties of the planet HATS-71b and its host star HATS-71.

In Section 2 we present the observations. We describe the analyses that we have performed to confirm the planetary system and determine its properties in Section 3. We conclude with a discussion of the results in Section 4.

2. Observations

2.1. Photometric Detection

HATS-71 was initially detected as a transiting planet candidate based on observations by the HATSouth network. A total of 26,668 observations were gathered at 4 min cadence between UT 2011 July 17 and UT 2012 October 25. The source was observed by the HS-1, HS-3, and HS-5 instruments (located in Chile, Namibia, and Australia, respectively) in HATSouth field G755, and by the HS-2, HS-4, and HS-6 instruments (located in Chile, Namibia, and Australia, respectively) in HATSouth field G756. Observations were carried out as described by Bakos et al. (2013), and reduced to trend-filtered light curves (filtered using the method of Kovács et al. 2005) and searched for transiting planet signals (using the box-fitting least squares or BLS method; Kovács et al. 2002) as described by Penev et al. (2013). We identified a periodic box-shaped transit signal in the trend-filtered light curve of HATS-71 with a period of 3.7955 days and a depth of 61.8 mmag. Based on this we selected the object as a candidate, assigning it the HATSouth candidate identifier HATS755-002. The trend-filtered HATSouth light curve has a residual rms of 50 mmag. The light curve is shown phase-folded in Figure 1, while the data are made available in Table 1.

We searched for additional periodic signals in the combined HATSouth light curve using both the generalized Lomb–Scargle (GLS) periodogram (Zechmeister & Kürster 2009) and the BLS algorithm, in both cases applied to the light curve after subtracting the best-fit transit model for HATS-71b. We find a peak in the GLS periodogram at a period of 41.72 ± 0.14 days with a false-alarm probability of 10^{-31} (Figure 2). This false-alarm probability is estimated using the relations from Zechmeister & Kürster (2009) appropriate for Gaussian white noise, but calibrated to the observed sampling and magnitude distribution via bootstrap simulations. The signal is independently detected in the G755 and G756 HATSouth light curves (with peak periods of 37.02 and 41.86 days, and false-alarm probabilities of 10^{-10} and 10^{-15} , respectively), which have similar time-coverage but were obtained with different instruments using different pointings on the sky. Fitting a

Table 1
Light Curve Data for HATS-71

BJD ^a (2400,000+)	Mag. ^b	σ_{Mag}	Mag. (orig.) ^c	Filter	Instrument
56186.87390	14.61050	0.02893	0.09177	<i>r</i>	HS/G755.4
56194.46534	14.46785	0.02515	-0.05088	<i>r</i>	HS/G755.4
56183.07906	14.53916	0.02462	0.02043	<i>r</i>	HS/G755.4
56202.05668	14.48734	0.03641	-0.03139	<i>r</i>	HS/G755.4
56167.89733	14.49451	0.02565	-0.02422	<i>r</i>	HS/G755.4
56141.32989	14.51297	0.03681	-0.00576	<i>r</i>	HS/G755.4
56213.44497	14.51480	0.02061	-0.00393	<i>r</i>	HS/G755.4
56114.76192	14.58036	0.04107	0.06163	<i>r</i>	HS/G755.4
56186.87727	14.53484	0.02796	0.01611	<i>r</i>	HS/G755.4
56145.12690	14.46642	0.02888	-0.05231	<i>r</i>	HS/G755.4

Notes.

^a Barycentric Julian Date computed on the TDB system with correction for leap seconds.

^b The out-of-transit level has been subtracted. For observations made with the HATSouth instruments (identified by “HS” in the “Instrument” column) these magnitudes have been corrected for trends using the EPD and TFA procedures applied *prior* to fitting the transit model. This procedure may lead to an artificial dilution in the transit depths when used in its plain mode, instead of the signal reconstruction mode (Kovács et al. 2005). The blend factors for the HATSouth light curves are listed in Table 4. For observations made with follow-up instruments (anything other than “HS” in the “Instrument” column), the magnitudes have been corrected for a quadratic trend in time, and for variations correlated with up to three PSF shape parameters, fit simultaneously with the transit.

^c Raw magnitude values without correction for the quadratic trend in time, or for trends correlated with the seeing. These are only reported for the follow-up observations.

(This table is available in its entirety in machine-readable form.)

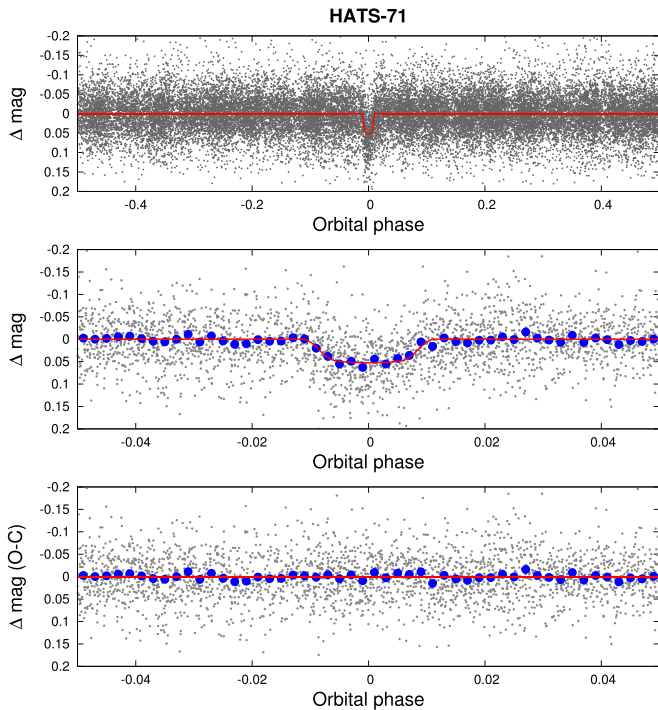


Figure 1. Phase-folded unbinned HATSouth light curve for HATS-71. Top: the full light curve. Middle: the light curve zoomed-in on the transit. Bottom: the residuals from the best-fit model zoomed-in on the transit. The solid line shows the model fit to the light curve. The dark filled circles show the light curve binned in phase with a bin size of 0.002.

sinusoid to the phase-folded data yields a semi-amplitude of 0.0134 ± 0.0039 mag. We interpret this period as the photometric rotation period of the star. Given the measured rotation period and stellar radius, the spectroscopic $v \sin i$ should be $< 0.625 \text{ m s}^{-1}$, i.e., undetectable even with the current high-resolution spectroscopy. Both the period and amplitude are

typical values for a field M3 dwarf star. No additional significant transit signals are detected by BLS in the combined HATSouth light curve. The highest peak in the BLS spectrum (other than the main transit with $P = 3.7955$ days) has a period of 82.7 days, a transit depth of 8.5 mmag, and a signal-to-noise ratio of only 4.5.

2.2. Spectroscopic Observations

Spectroscopic follow-up observations of HATS-71 were obtained with WiFeS on the Australian National University (ANU) 2.3 m (Dopita et al. 2007), the Planet Finder Spectrograph (PFS) on the Magellan 6.5 m (Crane et al. 2006, 2008, 2010), and Astronomy Research using the Cornell Infrared Imaging Spectrograph (ARCoIRIS) on the Blanco 4 m telescope (Abbott et al. 2016). The target was also observed with FEROS on the MPG 2.2 m (Kaufer & Pasquini 1998) between 2016 July 1 and 2016 September 16, but the spectra all had too low S/N to be of use.

The WiFeS observations of HATS-71, which were reduced following Bayliss et al. (2013), were used for reconnaissance of this faint M dwarf. We obtained a single spectrum at resolution $R \equiv \Delta \lambda / \lambda \approx 3000$ and S/N per resolution element of 18.9 on UT 2014 August 6 (Figure 3). We used this observation to estimate the atmospheric parameters of the star. The classification pipeline described by Bayliss et al. (2013) yielded parameters of $T_{\text{eff},*} = 3500 \pm 300$ K, $\log g = 4.7 \pm 0.3$ (cgs), and $[\text{Fe}/\text{H}] = 0.0 \pm 0.5$ dex, but a comparison to M dwarf standards indicates a somewhat lower temperature (Figure 3). Based on spectral matching to BT-Settl models (Allard et al. 2011) we estimate a temperature of 3350 K. The spectrum reveals this object to be a single-lined mid-M dwarf star with $v \sin i < 50 \text{ km s}^{-1}$. We also obtained four spectra at a resolution of $R \approx 7000$ between 2014 August 6–9, which we used to check for any large-amplitude RV variations. The spectra have an S/N between 5.9 and 21.2. The resulting radial

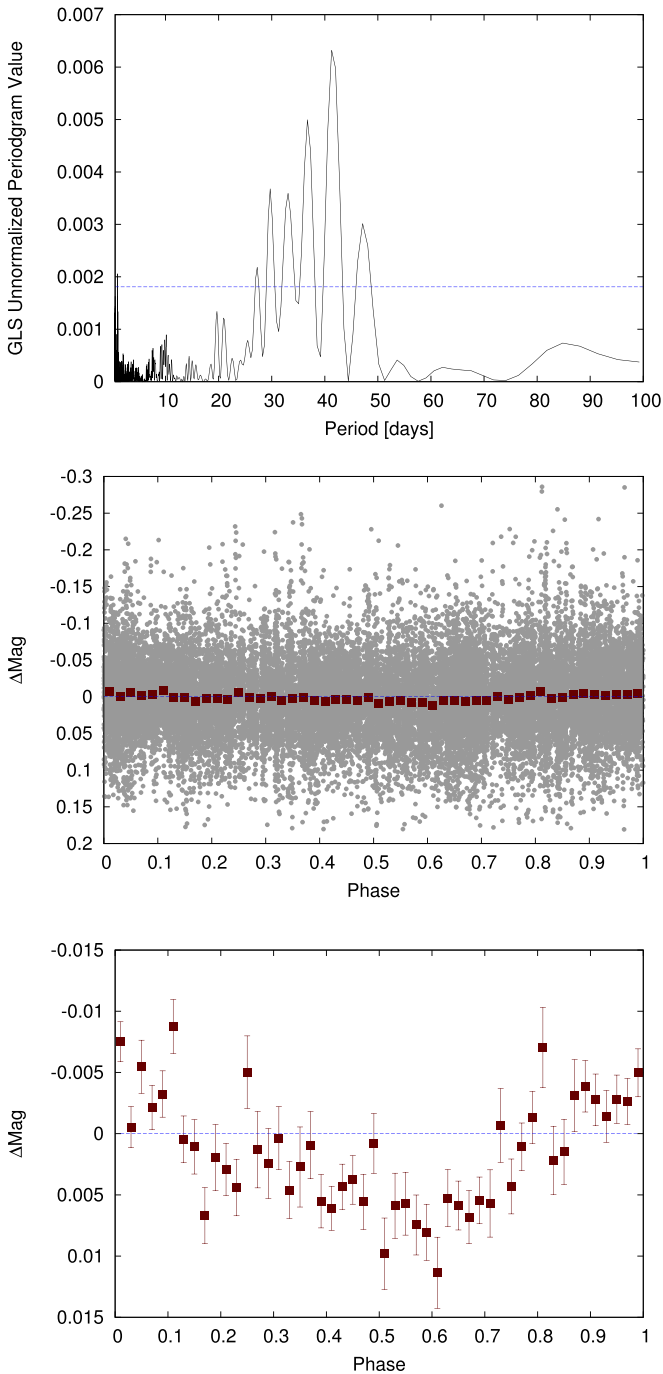


Figure 2. Top: GLS periodogram of the combined HATSouth light curve after subtracting the best-fit transit model for HATS-71b. The horizontal dashed blue line shows the false-alarm probability level of 10^{-5} . Middle: the HATSouth light curve phase-folded at the peak GLS period of 41.72 days. The gray points show the individual photometric measurements, while the dark red filled squares show the observations binned in phase with a bin size of 0.02. Bottom: same as the middle, but here we restrict the vertical range of the plot to better show the variation seen in the phase-binned measurements.

velocities have good phase coverage and an rms scatter of 2.3 km s^{-1} , comparable to the median per-point uncertainty of 2.9 km s^{-1} . The resulting upper limit on the mass of the transiting companion is $M_p < 31 M_J$ at 3σ confidence.

A total of eight PFS observations were obtained for HATS-71 between 2014 December 31 and 2017 January 13. These include seven observations through an I_2 absorption cell, and

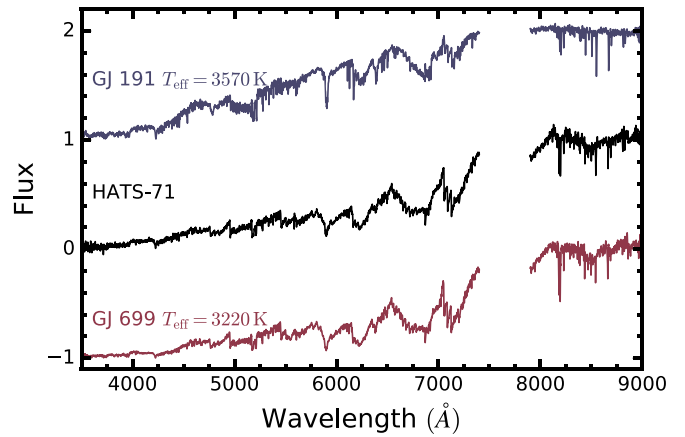


Figure 3. WiFeS/ANU 2.3 m $R = 3000$ optical spectra of HATS-71 (middle spectrum) and two other M dwarf standard stars for comparison. HATS-71 has the optical spectrum of an M3 dwarf star. The relative fluxes are on an arbitrary scale, and the two standard stars have been shifted vertically for clarity.

one observation without the cell, used to construct a template spectrum for use in the RV measurements. The observations were reduced to high-precision relative RV measurements following Butler et al. (1996), while spectral-line bisector spans (BSs) and their uncertainties were measured as described by Jordán et al. (2014) and Brahm et al. (2017a). To avoid excessive cosmic-ray contamination and smearing due to changes in time in the barycentric velocity correction, each observation was composed of two to four exposures, which were independently reduced and then co-added. The high-precision RV and BS measurements are shown phase-folded, together with the best-fit model, in Figure 4. Due to the faintness of the source, the RVs have a median per-point uncertainty of 17 m s^{-1} , which may be underestimated. The residuals from the best-fit model have an rms of 89 m s^{-1} (the observations themselves have an rms of 106 m s^{-1}). The BS measurements have an even larger scatter of 1.6 km s^{-1} , limiting their use in excluding scenarios involving blended eclipsing binaries (such scenarios are considered and rejected in Section 3.2).

We checked the PFS observations for $\text{H}\alpha$ emission, indicative of chromospheric activity, and found no evidence for this. If anything, $\text{H}\alpha$ is seen in absorption in these spectra.

The surface temperature of HATS-71 is too low to apply ZASPE (Brahm et al. 2017b), a synthetic-template-cross-correlation-based method to determine precise stellar atmospheric parameters, which we have used in analyzing most of the other planetary hosts discovered by HATSouth. For this reason we obtained a near-infrared spectrum of HATS-71 using the ARCoIRIS instrument on the Blanco 4 m at Cerro Tololo Inter-American Observatory (CTIO) in Chile (Abbott et al. 2016). This spectrum was used to determine $T_{\text{eff},*}$ and $[\text{Fe}/\text{H}]$.

ARCoIRIS is a cross-dispersed, single-object, long-slit, near-infrared spectrograph covering most of the wavelength range from 0.8 to $2.47 \mu\text{m}$, at a resolution of roughly 3500. ARCoIRIS spectra can only be taken in a single setup with a fixed slit assembly of $1''.1 \times 28''$. We observed HATS-71 using a pair of ABBA patterns (eight 100 s exposures in total) interleaved with hollow-cathode lamp spectra, and using HD 1860 as a telluric standard. The observations were carried out on UT 2016 July 15, and were reduced to wavelength- and telluric-corrected spectra using the standard SpeX-tool package (Cushing et al. 2004; Vacca et al. 2004). We note that we did

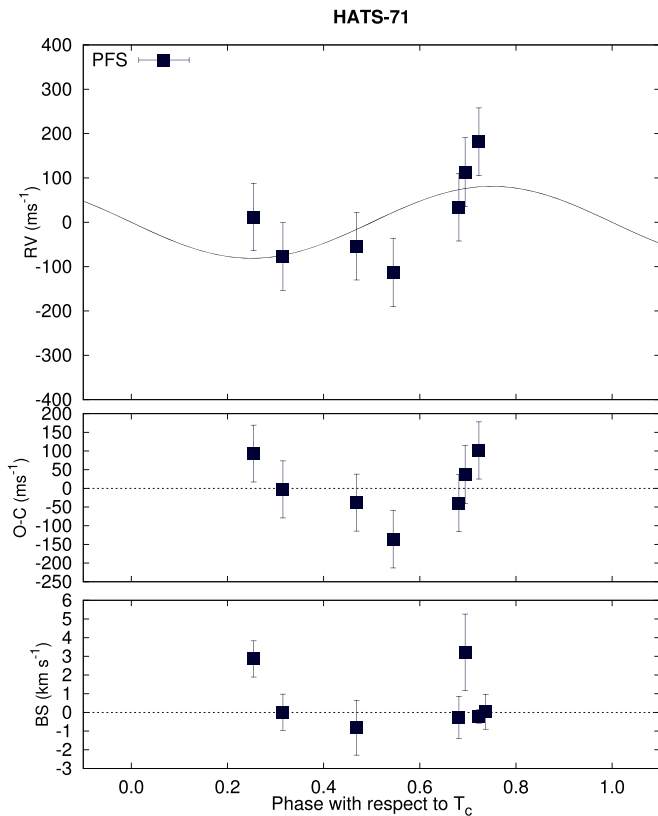


Figure 4. Phased high-precision RV measurements from PFS for HATS-71. Top: the phased measurements together with our best-fit model (see Table 4). Zero phase corresponds to the time of mid-transit. The center-of-mass velocity has been subtracted. Middle: the velocity $O - C$ residuals from the best fit. The error bars include the jitter term listed in Table 4 added in quadrature to the formal errors. Bottom: the phased BS. Note the different vertical scales of the panels.

not attempt to flux-calibrate our spectrum, as the observing conditions were not photometric. The data reduction resulted in six extracted orders, though we did not consider the sixth order in our analysis. Finally, we cut out regions strongly affected by telluric lines, normalized the spectra, and removed a second-order polynomial fit.

In order to estimate $T_{\text{eff}\star}$ and $[\text{Fe}/\text{H}]$ from our near-IR spectrum, we used the procedure described by Newton et al. (2015). These relations were calibrated using IRTF/SpeX spectra with a resolution of $R \sim 2000$, but ARCoIRS has a resolution of $R \sim 500$, therefore we downgraded our ARCoIRS spectra to the IRTF/SpeX resolution. In these downgraded spectra we measured the equivalent width of some selected lines and applied the relation from Newton et al. (2015). Based on this we measure $T_{\text{eff}\star} = 3500 \pm 120$ K and $[\text{Fe}/\text{H}] = 0.26 \pm 0.13$.

2.3. Ground-based Photometric Follow-up Observations

Follow-up ground-based photometric transit observations with higher precision were obtained for HATS-71 using the Danish 1.54 m telescope at La Silla Observatory in Chile (Andersen et al. 1995), 1 m telescopes from the Las Cumbres Observatory (LCOGT) network (Brown et al. 2013), a 0.32 m telescope at Hazelwood Observatory in Victoria, Australia, and a 0.36 m telescope at El Sauce Observatory in Chile. Three of the light curves were obtained through the TESS Follow-up Program (TFOP) following the independent detection of

HATS-71 as a candidate transiting planet system by the TESS team (see Section 2.4). All of the ground-based follow-up light curves are shown in Figure 5, while the data are available in Table 1.

An egress event was observed with the DFOSC camera on the Danish 1.54 m telescope on the night of UT 2014 October 5. A total of 51 images were collected at a median cadence of 225 s. The observations were carried out and reduced to a relative light curve following Rabus et al. (2016). The residuals from the best-fit transit model have a point-to-point rms of 2.4 mmag.

An ingress event was observed with the SBIG camera on one of the LCOGT 1 m telescopes at the South African Astronomical Observatory on UT 2014 October 24. A total of 39 images were collected at a median cadence of 76 s. We also observed a full transit with the sinistro camera on one of the LCOGT 1 m telescopes at CTIO on UT 2014 November 9. A total of 56 images were collected at a median cadence of 227 s. These observations were reduced to relative light curves as described in Hartman et al. (2015). A full transit was also observed through the TFOP program using the sinistro camera on one of the LCOGT 1 m telescopes at CTIO on UT 2018 September 17. A total of 44 images were collected at a median cadence of 163 s. These data were reduced to aperture photometry using the AstroImageJ software package (AIJ, Collins & Kielkopf 2013; Collins et al. 2017). The residuals from the best-fit transit model have a point-to-point rms of 15 mmag, 3.4 mmag, and 4.6 mmag on each of the respective nights.

An egress event was observed on UT 2018 September 13 at Hazelwood Observatory, a backyard observatory operated by Chris Stockdale in Victoria, Australia. The observations were carried out using a 0.32 m Planewave CDK12 telescope and an SBIG STT-3200 CCD imager. The images had a pixel scale of $1''.1$, while the average estimated point-spread function (PSF) FWHM on the night of the observations was $9''$. We include in the analysis the photometry measured from 28 images collected at a median cadence of 314 s. Aperture photometry was performed using AIJ. The residuals from the best-fit transit model have a point-to-point rms of 15 mmag.

A full transit was observed on UT 2018 September 17 at El Sauce Observatory in Chile by Phil Evans using a 0.36 m Planewave CDK14 telescope and an SBIG STT1603-3 CCD imager. These images had a pixel scale of $1''.47$, while the average estimate PSF FWHM on the night of the observations was $8''.2$. A total of 90 images are included in the analysis. The median cadence was 185 s. Aperture photometry was performed using AIJ. The residuals from the best-fit transit model have a point-to-point rms of 11 mmag.

2.4. Space-based Photometric Follow-up Observations

Photometric time-series observations of HATS-71 were carried out by the NASA TESS mission between 2018 July 25 and 2018 August 22 (Sector 1 of the mission).²⁹ The target (TIC 234523599) was selected for observations at 2 minute cadence through the TESS Guest Observer program.³⁰ The data were processed, and the source was identified as a candidate transiting planet system (denoted TOI 127.01) by the TESS

²⁹ Following the submission of the first draft of this paper, additional TESS observations of this system from Sector 2 were made public. We do not include these data in the analysis presented in Section 3.

³⁰ Program G011214, PI Bakos, “TESS Observations of Transiting Planet Candidates from HAT.”

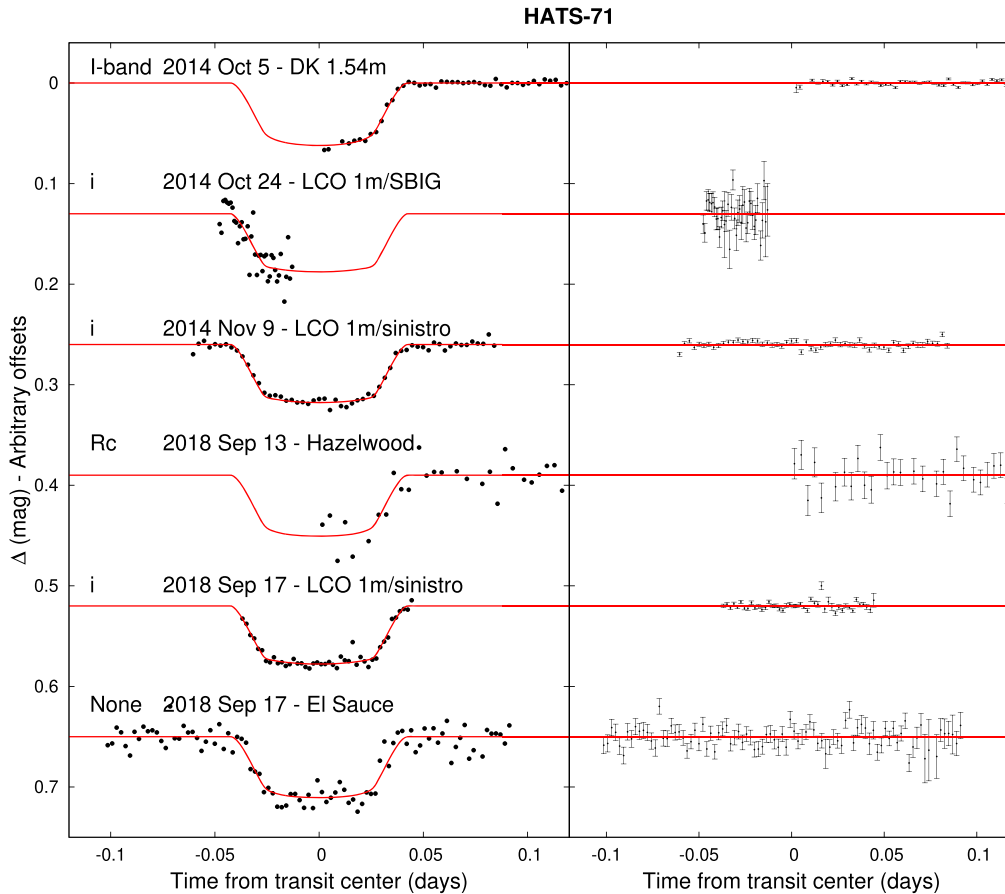


Figure 5. Unbinned, detrended, ground-based, follow-up transit light curves for HATS-71. The dates of the events, and filters and instruments used are indicated. Light curves following the first are displaced vertically for clarity. Our best fit from the global modeling described in Section 3.1 is shown by the solid lines. The residuals from the best-fit model are shown on the right-hand-side in the same order as the original light curves. The error bars represent the photon and background shot noise, plus the readout noise.

team following the methods described by Huang et al. (2018). We note that the identification of this object as a candidate by the TESS team was made independently of the observations described in the previous sections. Here we make use of the preliminary detrended light curve for HATS-71 produced by the TESS Science Processing Operations Center pipeline (based on Jenkins et al. 2016), which was included in the set of TESS alerts released to the public on 2018 September 5. Note that these Presearch Data Conditioning (PDC) light curves have not been arbitrarily detrended, but rather have had instrumental systematic signatures identified and removed using a multi-scale, maximum a posteriori approach (Smith et al. 2012; Stumpe et al. 2014). A total of eight consecutive primary transits, and six epochs of secondary eclipse are included in the light curve. The residuals from the best-fit model have a point-to-point rms of 16.5 mmag. The light curve is shown, together with the best-fit model, in Figure 6, while the time-series data are included in Table 1.

We searched for additional periodic signals in the TESS light curve in the same manner as we did for the HATSouth data (Section 2.1). No significant signals were found with either GLS or BLS in the TESS light curve after subtracting the best-fit transit model for HATS-71b. No evidence for the 41.72 ± 0.14 day photometric rotation period seen with HATSouth is observed in the TESS data, though this is hardly surprising, as this period exceeds the duration of the TESS

observations, and a long-term linear or quadratic trend could have been filtered out by the PDC pipeline. The highest peak in the BLS spectrum of the TESS residuals has a period of 9.06 days, a depth of 3.4 mmag, and a signal-to-noise ratio of only 5.4.

2.5. Search for Resolved Stellar Companions

In order to detect neighboring stellar companions we obtained z' -band high-spatial-resolution lucky imaging observations with the Astralux Sur imager (Hippler et al. 2009) on the New Technology Telescope (NTT) on the night of 2015 December 23. The observations were reduced as in Espinoza et al. (2016), and no neighbors were detected. The effective FWHM of the reduced image is 46.3 ± 5.5 mas. Figure 7 shows the resulting 5σ contrast curve. We may exclude neighbors with $\Delta z' < 2.5$ mag at $0''.2$, and $\Delta z' < 3.2$ mag at $1''$. We also note that there are no neighbors within $10''$ of HATS-71 in the Gaia DR2 catalog, based on which we rule out neighbors with $G \lesssim 20$ mag down to a limiting resolution of $\sim 1''$ (e.g., Ziegler et al. 2018).

3. Analysis

3.1. Joint Modeling of Observations

We analyzed the photometric and spectroscopic observations of HATS-71 following Hartman et al. (2019). The method

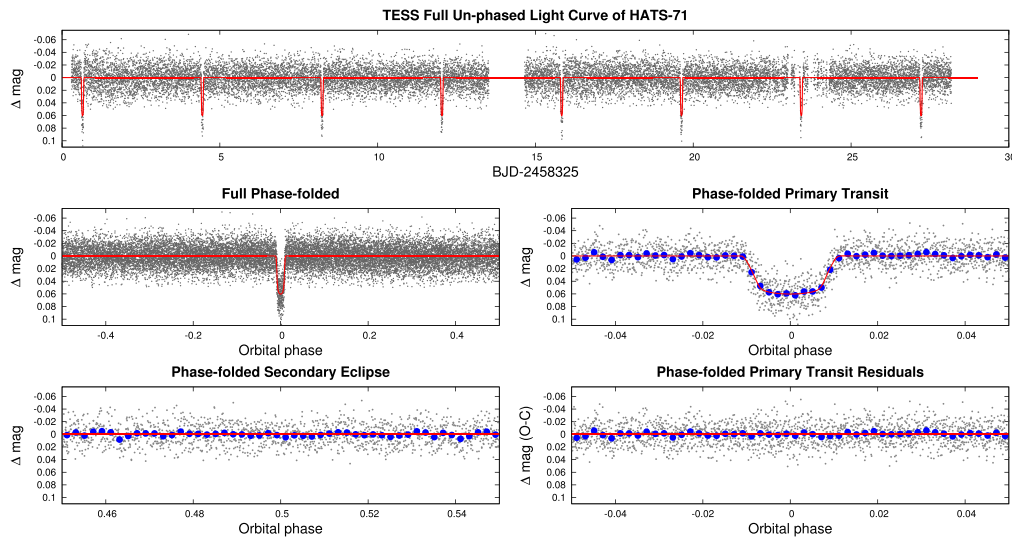


Figure 6. TESS unbinned Sector 1 light curve for HATS-71. We show the full unphased light curve as a function of time (top), the full phase-folded light curve (middle left), the phase-folded light curve zoomed-in on the primary transit (middle right), the phase-folded light curve zoomed-in on the secondary eclipse (bottom left), and the residuals from the best-fit model, phase-folded and zoomed-in on the primary transit (bottom right). The solid line in each panel shows the model fit to the light curve. The dark filled circles show the light curve binned in phase with a bin size of 0.002.

jointly fits all of the light curves, the RV observations, the Gaia DR2 parallax, the broadband photometry from Gaia DR2, Two Micron All Sky Survey (2MASS) (Skrutskie et al. 2006), APASS (Henden et al. 2015), and Wide-field Infrared Survey Explorer (WISE) (Cutri et al. 2014), and the spectroscopically determined $T_{\text{eff},*}$ and $[\text{Fe}/\text{H}]$ (here we use the values determined from the ARCoIRIS observations, Section 2.2). The PARSEC stellar evolution models (Marigo et al. 2017) are used in the fit to constrain the stellar properties. We adopt a Keplerian orbit to model the RV observations and light-curve models from Mandel & Agol (2002) in fitting the light curves, and we used a differential evolution Markov Chain Monte Carlo (DEMCMC) procedure to explore the fitness landscape and to determine the posterior distribution of the parameters. We made two changes to the procedure compared to what was done in Hartman et al. (2019): (1) we used a newer tabulation of the PARSEC models obtained through the color–magnitude diagram (CMD) v3.2 web-interface,³¹ which notably includes a revision to the bolometric corrections calculated for the Gaia bandpass (Maíz Apellániz & Weiler 2018); and (2) we varied the quadratic limb-darkening coefficients in the fit, taking the tabulated values from Claret et al. (2012, 2013) and Claret (2018) as priors.

We attempted to model the observations using the empirical method for determining the physical properties of the host star described in Hartman et al. (2019) (and similar to that of Stassun et al. 2018), rather than using the PARSEC stellar evolution models, but found that this provided a slightly worse fit to the data than using the PARSEC models. Most likely this is due to differences in how we interpolated the bolometric corrections compared to what is done in producing the PARSEC models.

In carrying out the analysis we assumed a circular orbit. Note that if the orbit is eccentric, the stellar density inferred from the light curve would be systematically different from what we measured here, which would in turn affect the stellar mass measurement and the inferred planetary mass limits. A solution

can be found, for example, with $e = 0.413$, which passes nicely through the RV observations and is consistent with the host star having a mass of $0.46 M_{\odot}$ and radius of $0.45 R_{\odot}$, and the planet having a mass of $1.68 M_{\text{J}}$ and radius of $0.94 R_{\text{J}}$. The limited number of RV observations gathered, however, prevents us from putting a believable constraint on the eccentricity from the data. Additional RV measurements are required, but are expensive due to the faintness of the host star.

In fitting the Danish 1.54 m follow-up light curve we included the light curves for 10 neighboring stars as trend filtering algorithm (TFA) templates to account for systematic drifts in the photometry shared by some of the comparisons that were not well modeled by a simple function of time. For the other ground-based follow-up light curves, where systematic variations were less pronounced, we included only a quadratic function in time to account for trends.

In an earlier version of this paper, which has been made public on the arXiv server, we used the MWDUST model (Bovy et al. 2016) to place a prior constraint on the extinction, and did not include the WISE photometry in the analysis. In that case we found that the host star HATS-71 had a luminosity greater than most main-sequence stars at the measured temperature, and greater than the highest metallicity isochrones tabulated in the PARSEC isochrones interpolated using CMD v3.1. We found that modeling the system as a single star with a planet together with an unresolved late M dwarf stellar companion provided the best fit to the data. Because the WISE bandpasses have minimal extinction, including them in the analysis allows for a direct measurement of A_V . Our latest analysis also makes use of new theoretical models of the Gaia bandpass, as incorporated into CMD v3.2, which has a noticeable effect on the predicted $\text{BP}_0\text{--RP}_0$ and G_{abs} isochrones for mid-M dwarf stars as a function of metallicity. In our latest analysis we find that the observations are best fit by a single star with a transiting planet, and that $A_V = 0.033 \pm 0.011$ mag, which is slightly lower than the expected value of $A_V = 0.041$ mag from the MWDUST model. We find that the updated theoretical model provides a better match to the high-precision measurements

³¹ <http://stev.oapd.inaf.it/cgi-bin/cmd>

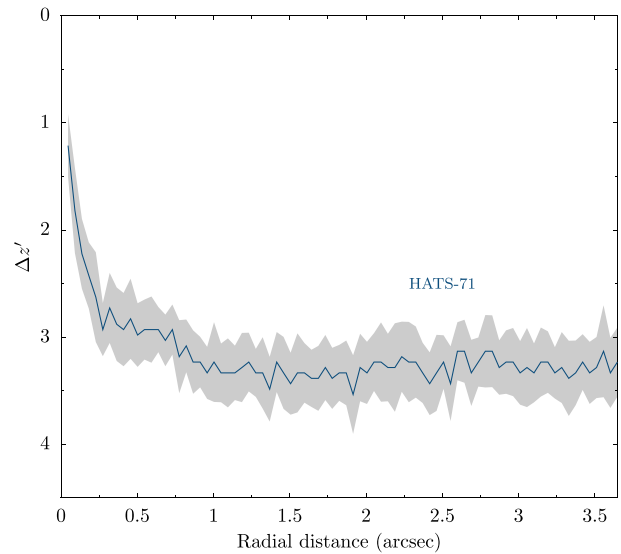
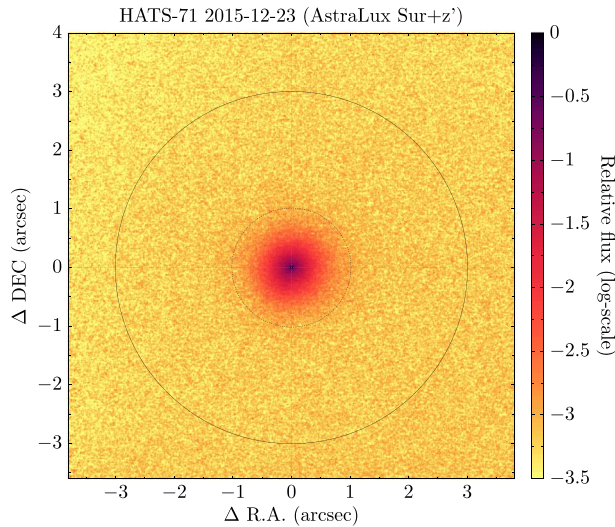


Figure 7. Left: Astralux Sur z' image of HATS-71 showing no apparent neighbors. Right: 5σ contrast curve for HATS-71 based on our Astralux Sur z' observation. The gray band shows the variation in the limit in azimuth at a given radius.

of color, density, and absolute magnitude that are available for HATS-71 than what was found in our prior analysis.

In Figure 8 we show the H-R diagram using the extinction- and distance-corrected Gaia DR2 BP₀–RP₀ and G_{abs} measurements. Here we show the measurements for HATS-71 as well as for all stars in the Gaia DR2 catalog in a $10^\circ \times 10^\circ$ box centered on HATS-71 with parallax $\varpi > 7$ mas, $\sigma_\varpi < 0.2$ mas, and BP, RP, and G all measured to greater than 10σ confidence, and with $1.5 < \text{BP} - \text{RP}_0 < 3.5$ and $7.0 < G_{\text{abs}} < 12.0$. We also show theoretical PARSEC isochrones for a range of ages and metallicities, and the median main-sequence relation based on the selected stars from the Gaia DR2 sample. HATS-71 is consistent with the theoretical relation calculated at the spectroscopically measured metallicity.

Figure 9 shows the broadband spectral energy distribution (SED) for HATS-71 together with our fit to the observations. We found that the model SED was unable to reproduce the observations to within their uncertainties. Especially problematic are the very precise Gaia DR2 measurements (systematic uncertainties are estimated at 0.002 mag, 0.005 mag, and 0.003 mag for the G , BP, and RP bands, respectively). To account for this, we included an extra error term of 0.057 mag, which we added in quadrature to the broadband photometry measurements, such that $\chi^2/\text{dof} = 1$ about the best fit when excluding the W3 measurement. This is meant to capture the systematic uncertainties in the theoretical models. Figure 9 shows both the observational uncertainties and the uncertainties including the additional systematic error.

Previous work has shown that rapidly rotating, magnetically active M dwarfs often have lower surface temperatures and larger radii than predicted by theoretical stellar evolution models (e.g., see the recent work by Jaehnig et al. 2019 and Somers & Stassun 2017 investigating the inflation of M dwarfs in the Hyades and Pleiades; see also references therein for a rich literature on this topic). HATS-71, however, does not exhibit H α emission typical of magnetically active M dwarfs, and its measured photometric rotation period of 41.72 ± 0.14 days (Section 2.1) is substantially longer than the periods of M dwarf stars for which radius inflation is typically observed ($P_{\text{rot}} \lesssim 10$ days), so we expect the radius of

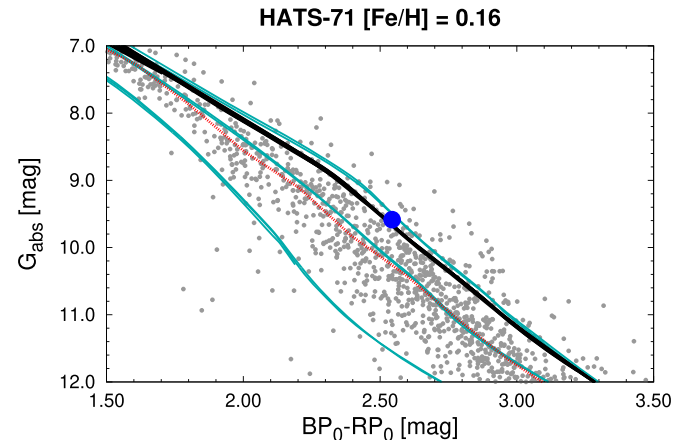


Figure 8. Hertzsprung–Russell diagram constructed from the Gaia DR2 photometry corrected for distance and extinction. The blue filled circle shows HATS-71 (the uncertainties are smaller than the size of the circle), while the gray filled circles show other stars in Gaia DR2 with $\varpi < 7$ mas and within a $10^\circ \times 10^\circ$ box centered on HATS-71. Overplotted are PARSEC model isochrones for metallicities of -0.5 (left set of cyan lines), 0 (middle set of cyan lines), $+0.4414$ (right set of cyan lines), and the spectroscopically estimated metallicity of 0.26 dex (black lines). At each metallicity we show models for ages 1.0, 5.0, and 12.0 Gyr, though the difference with age at fixed metallicity is negligible at the scale shown here. We also show the median main-sequence relation based on the Gaia DR2 stars included in the plot (red line).

HATS-71 to be in agreement with the theoretical models in this case.

The measured astrometric, spectroscopic, and photometric parameters of HATS-71 are collected in Table 2. Table 3 gives the stellar parameters that are derived through the modeling discussed in this section, Table 4 gives the planetary parameters derived through this modeling, while Table 5 shows the high-precision RV and BS measurements for HATS-71.

We find that, thanks largely to Gaia DR2, the star HATS-71 has a tightly constrained radius of $0.4783 \pm 0.0060 R_\odot$. Based on our analysis we also find a stellar mass of $0.4861 \pm 0.0060 M_\odot$. For comparison, using the mass– M_K relation of Delfosse et al. (2000) gives an estimated stellar mass of $0.455 M_\odot$, while using that of Benedict et al. (2016) gives an estimated stellar mass of $0.50 M_\odot$.

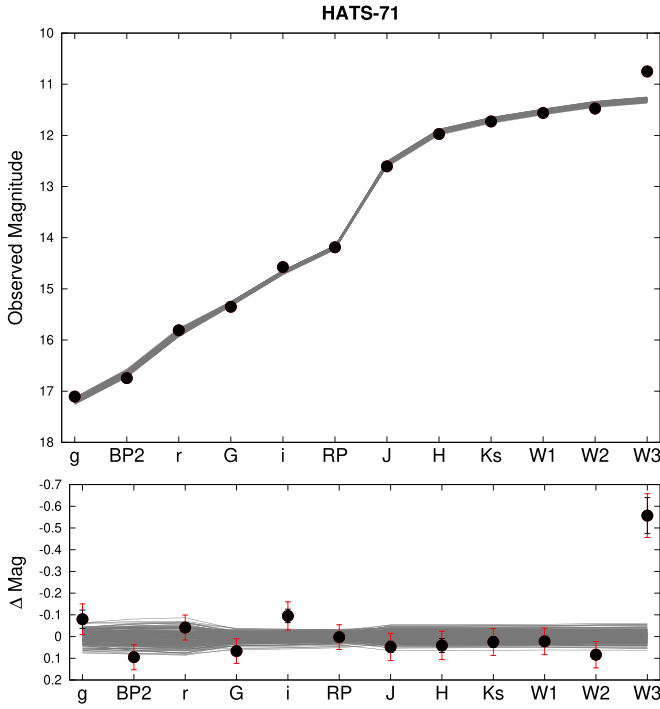


Figure 9. Broadband SED for HATS-71 based on catalog photometry from Gaia DR2, APASS, 2MASS, and WISE. Top: the observed magnitudes in each filter (black filled circles) are shown together with 200 model curves (gray lines) drawn at random from the posterior distribution produced by our DEMCMC analysis (Section 3.1). Bottom: the residuals from the best-fit model. The black error bars on each point are the observational uncertainties including best estimates of the systematic errors. The red error bars include an additional error of 0.057 mag added in quadrature to the observational uncertainties. This additional error is meant to capture systematic errors in the theoretical models for the SED, and is necessary because the theoretical models are unable to reproduce the observations to within their formal uncertainties. Even with this additional error, the models are unable to reproduce the W3 observation, which is brighter by ~ 0.5 mag than predicted.

Both of these estimates are reasonably close to the value determined from our modeling.

We find that the planet HATS-71b has a radius of $1.024 \pm 0.018 R_J$. Due to the faintness of the source, we are unable to determine the mass of the planet with greater than 2σ confidence. Our modeling yields a mass of $0.37 \pm 0.24 M_J$, with a 95% confidence upper limit of $M_p < 0.81 M_J$. The planet has an estimated equilibrium temperature (assuming full redistribution of heat and zero albedo) of 586.8 ± 2.3 K.

The 89 m s^{-1} scatter in the PFS RV residuals is significantly larger than the median per-point uncertainty of 17 m s^{-1} . Given the limited number of RVs obtained, we cannot say whether this is due to the planet having a significant eccentricity, stellar activity, additional planets in the system, or our underestimating the uncertainties in these low S/N spectra. In modeling the data we incorporated a jitter term, which we added in quadrature to the formal uncertainties and varied in the fit. We find a jitter of $95 \pm 40 \text{ m s}^{-1}$ is needed to explain the excess scatter. If the orbit is eccentric, the jitter could be as low as 37 m s^{-1} .

3.2. Blend Analysis

In order to rule out the possibility that HATS-71 is a blended stellar eclipsing binary system, we carried out a blend analysis of the photometric data following Hartman et al. (2019). In this

Table 2
Astrometric, Spectroscopic, and Photometric Parameters for HATS-71

Parameter	Value	Source
Astrometric properties and cross-identifications		
2MASS-ID	01021226-6145216	
TIC-ID	TIC 234523599	
Gaia DR2-ID	4710594412266148352	
R.A. (J2000)	$01^{\text{h}}02^{\text{m}}12^{\text{s}}.2812$	Gaia DR2
Decl. (J2000)	$-61^{\circ}45'21''.6599$	Gaia DR2
$\mu_{\text{R.A.}}$ (mas yr^{-1})	78.858 ± 0.087	Gaia DR2
$\mu_{\text{decl.}}$ (mas yr^{-1})	-27.095 ± 0.064	Gaia DR2
Parallax (mas)	7.103 ± 0.043	Gaia DR2
Spectroscopic properties		
$T_{\text{eff}\star}$ (K)	3500 ± 120	ARCoIRIS ^a
[Fe/H]	0.26 ± 0.13	ARCoIRIS
γ_{RV} (m s^{-1})	24.1 ± 1.4	WiFeS ^b
Photometric properties		
P_{rot} (days)	41.72 ± 0.14	HATSouth
G (mag) ^c	15.35120 ± 0.00050	Gaia DR2
BP (mag) ^c	16.7435 ± 0.0038	Gaia DR2
RP (mag) ^c	14.1873 ± 0.0013	Gaia DR2
g (mag)	17.105 ± 0.042	APASS ^d
r (mag)	15.8100 ± 0.0090	APASS ^d
i (mag)	14.575 ± 0.031	APASS ^d
J (mag)	12.605 ± 0.026	2MASS
H (mag)	11.972 ± 0.032	2MASS
K_s (mag)	11.727 ± 0.025	2MASS
W1 (mag)	11.561 ± 0.022	WISE
W2 (mag)	11.475 ± 0.021	WISE
W3 (mag)	10.751 ± 0.083	WISE

Notes.

^a ARCoIRIS instrument on the Blanco 4 m at CTIO (Abbott et al. 2016).

^b The error on γ_{RV} is determined from the orbital fit to the RV measurements and does not include the systematic uncertainty in transforming the velocities to the IAU standard system. The velocities have not been corrected for gravitational redshifts.

^c The listed uncertainties for the Gaia DR2 photometry are taken from the catalog. For the analysis we assume additional systematic uncertainties of 0.002 mag, 0.005 mag, and 0.003 mag for the G , BP, and RP bands, respectively.

^d From APASS DR6 as listed in the UCAC 4 catalog (Zacharias et al. 2013).

Table 3
Derived Stellar Parameters for the HATS-71 System

Parameter	Value
M_{\star} (M_{\odot})	0.4861 ± 0.0060
R_{\star} (R_{\odot})	0.4783 ± 0.0060
$\log g_{\star}$ (cgs)	4.7653 ± 0.0067
ρ_{\star} (g cm^{-3})	6.26 ± 0.17
L_{\star} (L_{\odot})	0.02755 ± 0.00061
$T_{\text{eff}\star}$ (K)	3405 ± 10
[Fe/H] (dex)	0.170 ± 0.036
Age (Gyr)	$3.2^{+3.8}_{-1.5}$
A_V (mag)	0.033 ± 0.011
Distance (pc)	140.91 ± 0.80

Notes. The listed parameters are those determined through the joint differential evolution Markov Chain analysis described in Section 3.1. Systematic errors in the stellar evolution models are not included, and likely dominate the error budget. The constraint from these models leads to very low formal uncertainties on parameters such as $T_{\text{eff}\star}$.

Table 4
Orbital and Planetary Parameters for HATS-71b

Parameter	Value
Light-curve parameters	
P (days)	3.7955202 ± 0.0000010
T_c (BJD) ^a	$2457, 858.80134 \pm 0.00023$
T_{14} (days) ^a	0.08395 ± 0.00062
$T_{12} = T_{34}$ (days) ^a	0.01692 ± 0.00049
a/R_*	16.84 ± 0.15
ζ/R_* ^b	29.72 ± 0.34
R_p/R_*	0.2202 ± 0.0024
b^2	$0.121^{+0.024}_{-0.027}$
$b \equiv a \cos i/R_*$	$0.348^{+0.033}_{-0.042}$
i (deg)	88.82 ± 0.13
Limb-darkening coefficients ^c	
c_1, r	0.34 ± 0.15
c_2, r	0.26 ± 0.18
c_1, R	0.24 ± 0.11
c_2, R	0.34 ± 0.17
c_1, i	0.19 ± 0.10
c_2, i	0.10 ± 0.16
c_1, I	0.28 ± 0.14
c_2, I	0.25 ± 0.17
c_1, T	0.25 ± 0.12
c_2, T	0.19 ± 0.17
RV parameters	
K (m s^{-1})	77 ± 50
RV jitter PFS (m s^{-1}) ^d	95 ± 40
Planetary parameters	
M_p (M_J)	0.37 ± 0.24
R_p (R_J)	1.024 ± 0.018
$C(M_p, R_p)$ ^e	-0.03
ρ_p (g cm^{-3})	0.42 ± 0.28
$\log g_p$ (cgs)	$2.94^{+0.21}_{-0.31}$
a (au)	0.03745 ± 0.00015
T_{eq} (K)	586.8 ± 2.3
Θ ^f	0.055 ± 0.035
$\log_{10}\langle F \rangle$ (cgs) ^g	7.4272 ± 0.0070

Notes. Parameters are determined as described in Section 3.1 assuming HATS-71 is a single star with a transiting planet on a circular orbit.

^a Times are in Barycentric Julian Date computed on the TDB system with correction for leap seconds. T_c : Reference epoch of mid-transit that minimizes the correlation with the orbital period. T_{12} : total transit duration, time between first and last contact; $T_{12} = T_{34}$: ingress/egress time, time between first and second, or third and fourth contact.

^b Reciprocal of the half-duration of the transit used as a jump parameter in our MCMC analysis in place of a/R_* . It is related to a/R_* by the expression $\zeta/R_* = (a/R_*)[2\pi(1 + e \sin \omega)]/(P\sqrt{1 - b^2}\sqrt{1 - e^2})$ (Bakos et al. 2010).

^c Values for a quadratic law. These parameters are varied in the fit, using the tabulations from Claret et al. (2012, 2013) and Claret (2018) to place a prior constraint on their values.

^d Term added in quadrature to the formal RV uncertainties for each instrument. This is treated as a free parameter in the fitting routine for the “single star” model.

^e Correlation coefficient between the planetary mass M_p and radius R_p estimated from the posterior parameter distribution. This was not estimated for the “binary star” model.

^f The Safronov number is given by $\Theta = \frac{1}{2}(V_{\text{esc}}/V_{\text{orb}})^2 = (a/R_p)(M_p/M_*)$ (see Hansen & Barman 2007).

^g Incoming flux per unit surface area, averaged over the orbit.

Table 5
Relative Radial Velocities and Bisector Spans from PFS/Magellan for HATS-71

BJD (2450,000+)	RV ^a (m s^{-1})	σ_{RV} ^b (m s^{-1})	BS (m s^{-1})	σ_{BS} (m s^{-1})	Phase
7022.57729	52.41	16.56	-264.3	1123.8	0.681
7025.56597	-35.74	15.91	-816.3	1469.2	0.469
7026.58472	33.9	932.1	0.737
7325.69973	-95.44	19.13	0.545
7385.55818	-58.94	17.33	6.7	970.8	0.315
7614.83615	199.77	17.52	-220.5	358.3	0.723
7616.85346	30.21	15.83	2859.9	969.4	0.254
7766.54828	131.18	22.78	3214.5	2049.4	0.694

Notes.

^a The zero-point of these velocities is arbitrary. An overall offset γ fitted to the velocities has been subtracted.

^b Internal errors excluding the component of astrophysical jitter considered in Section 3.1.

(This table is available in machine-readable form.)

analysis we model the photometric and spectroscopic observations of HATS-71 under four different scenarios: a single star with a planet (referred to as the H-p model following the nomenclature from Hartman et al. 2009), a hierarchical triple star system where the two fainter stars form an eclipsing binary (referred to as the H, S-s model), a blend between a bright foreground star and a fainter background eclipsing binary star system (referred to as the H, S-S_{BGEB} model), and a bright star with a transiting planet and a fainter unresolved stellar companion (referred to as the H-p, s model). Note that the APASS and WISE W3 photometric observations were not included in this analysis, but we expect their impact to be negligible and with no effect on the conclusions regarding whether or not the system is a blend of stars. We find that in performing the analysis described in Section 3.1, including these observations makes only a small change to the derived stellar mass and radius compared to not including them.

We find that the best-fitting model is the H-p model, which yields $\Delta\chi^2 = -14, -79, \text{ and } -216$ compared to the best-fit H-p, s model, H, S-S_{BGEB} model, and H, S-s model, respectively. We can clearly rule out both the H, S-s and H, S-S_{BGEB} blended stellar eclipsing binary models based on this analysis. The lack of any stellar companion detected in high-resolution imaging (Section 2.5), or large-amplitude spectral-line BS variations provides further evidence against these scenarios of blended stellar eclipsing binaries. The H-p, s model is also disfavored, and we can exclude at 95% confidence an unresolved stellar companion with a luminosity ratio compared to the planet-hosting star of $L_B/L_A > 0.11$ or with a mass $M_B > 0.18 M_{\odot}$.

4. Discussion

The discovery of HATS-71b demonstrates that, at least in some cases, Jupiter-sized planets are able to form and migrate around stars with masses as low as HATS-71 ($0.4861 \pm 0.0060 M_{\odot}$). It remains to be seen whether such planets occur with the same frequency as they do around solar-type stars (i.e., $0.43\% \pm 0.05\%$).

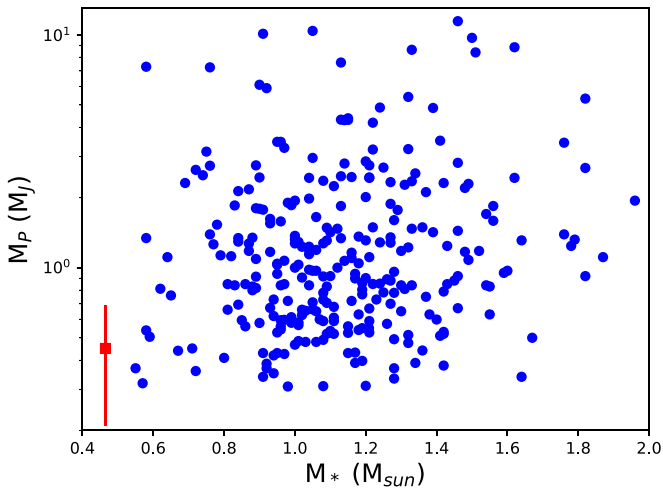


Figure 10. Planet mass as a function of host star mass for all known giant ($M_p > 0.3 M_J$) planets with measured masses and radii (blue circles) and for HATS-71b (red square with error bars). Data from NASA Exoplanet Archive as of 2018 October 4.

Fressin et al. 2013) or whether giant planet formation is rarer around low-mass stars as predicted by core accretion theory (e.g., Laughlin et al. 2004; Liu et al. 2016). Figure 10 shows giant planet masses as a function of host star mass for systems with measured planetary masses. HATS-71b is the giant planet with the lowest host star mass that has been discovered to date. The sparsity of systems with host masses $< 0.5 M_\odot$ is apparent from Figure 10, although this may just be a reflection of the fact that most of the surveys contributing to the discoveries shown did not monitor sufficient numbers of low-mass stars. Over the next two years of HATSouth and TESS discoveries, we should gain a better statistical understanding of these systems.

The deep transits that these systems present make photometric detection relatively robust in both the HATSouth and TESS survey data. Indeed, the 4.7% transit for HATS-71b makes this the deepest transit observed by a hot Jupiter (as defined in the Introduction). In Figure 11 we show the transit depths of these planets as a function of period, where the depths were calculated from the planetary radius R_p , stellar radius R_* , impact parameter b , eccentricity e , and argument of periastron of the orbit ω (whenever available), also taking into account the grazing nature of some orbits. The second and third deepest transits are Qatar-4b (3.4%; Alsubai et al. 2017) and HATS-6b (3.3%; Hartman et al. 2015).

However, RV follow-up is extremely challenging since such stars are generally faint at visible wavelengths where most high-precision spectrographs operate. The spectra of these stars may also be less amenable to measuring precise RV variations, because they are dominated by broader molecular absorption features rather than the narrow metal lines in solar-type stars (see Figure 3). A new generation of stable IR spectrographs will measure precise radial velocities in order to search for planets orbiting M dwarfs, and these include CARMENES (Quirrenbach et al. 2014), SPIROU (Artigau et al. 2014), IRD (Kotani et al. 2014), HPF (Wright et al. 2018), NIRPS (Wildi et al. 2017), and GIARPS (Claudi et al. 2018).

Such measurements may provide another avenue for RV follow-up of transiting giant planets orbiting M dwarfs. However, we note that for mid-M dwarfs such as HATS-71, optical spectroscopy will probably remain the best source of

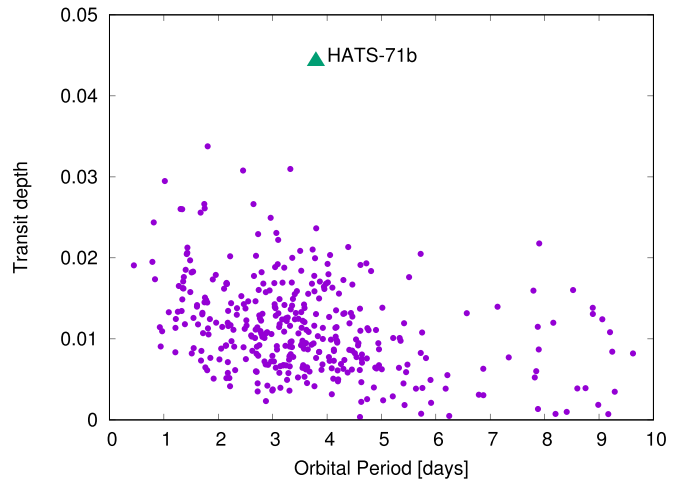


Figure 11. Transit depth as a function of orbital period for hot Jupiters. The depth was calculated from the planetary radius R_p , stellar radius R_* , impact parameter b , eccentricity e , and argument of periastron of the orbit ω (whenever available), also taking into account the grazing nature of some orbits. Data were taken from exoplanet.eu.

high-precision radial velocities. For the CARMENES spectrograph, which hosts both optical and IR arms, it appears that the RV precision is still higher in the optical wavelengths until spectral types of M8 or later (Reiners et al. 2018).

The deep transits will facilitate atmospheric characterization of the planet using transmission spectroscopy. We estimate that the transmission signature could be anywhere from 300 to 700 ppm, assuming that the cloud properties of hot Jupiters around M stars are similar to those around F, G, and K stars. Atmospheric characterization might be used instead of radial velocities to get the mass of the planet via MassSpec (de Wit & Seager 2013), although note the ambiguities detailed in Batalha et al. (2017).

HATS-71 was observed by the TESS spacecraft with 2 minute cadence as a candidate from the HATSouth Guest Observer Program (GO11214; PI Bakos). Due to the high-precision ground-based light curves that had already been obtained in 2014 using 1 m class telescopes (see Section 2.3), the addition of the TESS light curve did not have a significant impact on parameters such as the planetary radius or the orbital ephemerides. However, the TESS light curve did contain the best photometry available at phase 0.5, which allowed us to rule out a secondary eclipse with much higher confidence. With many hundreds of transiting planet candidates, follow-up photometry that covers both the primary transit and any possible secondary eclipse is a time-consuming and resource-intensive task. The use of TESS light curves to help confirm existing candidates is therefore an obvious synergy between HATSouth and TESS, and this method will continue to be adopted for future TESS sectors.

Development of the HATSouth project was funded by NSF MRI grant NSF/AST-0723074, operations have been supported by NASA grants NNX09AB29G, NNX12AH91H, and NNX17AB61G, and follow-up observations have received partial support from grant NSF/AST-1108686. G.Á.B. wishes to thank Konkoly Observatory of the Hungarian Academy of Sciences for their warm hospitality during numerous visits during the past years, in particular the Distinguished Guest Fellow program. A.J. acknowledges support from FONDECYT project

1171208, BASAL CATA AFB-170002, and project IC120009 “Millennium Institute of Astrophysics (MAS)” of the Millennium Science Initiative, Chilean Ministry of Economy. N.E. is supported by CONICYT-PCHA/Doctorado Nacional. R.B. acknowledges support from FONDECYT Post-doctoral Fellowship Project No. 3180246. N.E. acknowledges support from project IC120009 “Millennium Institute of Astrophysics (MAS)” of the Millennium Science Initiative, Chilean Ministry of Economy. L.M. acknowledges support from the Italian Minister of Instruction, University and Research (MIUR) through FFABR 2017 fund. L.M. acknowledges support from the University of Rome Tor Vergata through “Mission: Sustainability 2016” fund. V.S. acknowledges support form BASAL CATA PFB-06. A.V. is supported by the NSF Graduate Research Fellowship, grant No. DGE 1144152.

Based on observations at Cerro Tololo Inter-American Observatory, National Optical Astronomy Observatory (NOAO Prop. ID 2016A/CN-615, 2016B-CN0908, 2017A-C79, 2017B-0909, 2018A-CN46/908; PI: Rabus), which is operated by the Association of Universities for Research in Astronomy (AURA) under a cooperative agreement with the National Science Foundation. M.R. acknowledges support from CONICYT project Basal AFB-170002.

















This paper also makes use of observations from the LCOGT network. Some of this time was awarded by NOAO. We acknowledge the use of the AAVSO Photometric All-Sky Survey (APASS), funded by the Robert Martin Ayers Sciences Fund, and the SIMBAD database, operated at CDS, Strasbourg, France. This work has made use of data from the European Space Agency (ESA) mission Gaia (<https://www.cosmos.esa.int/gaia>), processed by the Gaia Data Processing and Analysis Consortium (DPAC, <https://www.cosmos.esa.int/web/gaia/dpac/consortium>). Funding for the DPAC has been provided by national institutions, in particular the institutions participating in the Gaia Multilateral Agreement. This research has made use of the NASA Exoplanet Archive, which is operated by the California Institute of Technology, under contract with the National Aeronautics and Space Administration under the Exoplanet Exploration Program. We acknowledge the use of TESS Alert data, which is currently in a beta test phase, from pipelines at the TESS Science Office and at the TESS Science Processing Operations Center. This paper includes data collected by the TESS mission, which are publicly available from the Mikulski Archive for Space Telescopes (MAST). Finally, G.Á.B. wishes to thank Princeton’s AST205 class for all the inspiration they gave during the fall semester of 2018.

Facilities: HATSouth, ATT (WiFeS), Magellan:Clay (PFS), Blanco (ARCoIRIS), Danish 1.54 m Telescope (DFOSC), LCOGT, NTT (Astralux Sur), TESS, Gaia, Exoplanet Archive.

Software: FITSH (Pál 2012), BLS (Kovács et al. 2002), VARTOOLS (Hartman & Bakos 2016), CERES (Brahm et al. 2017a), AstroImageJ (Collins & Kielkopf 2013; Collins et al. 2017), SPEX-tool (Cushing et al. 2004; Vacca et al. 2004), SExtractor (Bertin & Arnouts 1996), Astrometry.net (Lang et al. 2010), MWDUST (Bovy et al. 2016).

ORCID iDs

G. Á. Bakos  <https://orcid.org/0000-0001-7204-6727>
 D. Bayliss  <https://orcid.org/0000-0001-6023-1335>
 J. Bento  <https://orcid.org/0000-0002-9832-9271>
 W. Bhatti  <https://orcid.org/0000-0002-0628-0088>
 R. Brahm  <https://orcid.org/0000-0002-9158-7315>
 N. Espinoza  <https://orcid.org/0000-0001-9513-1449>

J. D. Hartman  <https://orcid.org/0000-0001-8732-6166>
 A. Jordán  <https://orcid.org/0000-0002-5389-3944>
 L. Mancini  <https://orcid.org/0000-0002-9428-8732>
 K. Penev  <https://orcid.org/0000-0003-4464-1371>
 M. Rabus  <https://orcid.org/0000-0003-2935-7196>
 P. Sarkis  <https://orcid.org/0000-0001-8128-3126>
 V. Suc  <https://orcid.org/0000-0001-7070-3842>
 M. de Val-Borro  <https://orcid.org/0000-0002-0455-9384>
 G. Zhou  <https://orcid.org/0000-0002-4891-3517>
 R. P. Butler  <https://orcid.org/0000-0003-1305-3761>
 J. Crane  <https://orcid.org/0000-0002-5226-787X>
 S. Durkan  <https://orcid.org/0000-0002-3663-3251>
 R. Vanderspek  <https://orcid.org/0000-0001-6763-6562>
 D. W. Latham  <https://orcid.org/0000-0001-9911-7388>
 J. N. Winn  <https://orcid.org/0000-0002-4265-047X>
 C. Stockdale  <https://orcid.org/0000-0003-2163-1437>

References

- Abbott, T. M. C., Walker, A. R., Points, S. D., et al. 2016, *Proc. SPIE*, 9906, 99064D
- Allard, F., Homeier, D., & Freytag, B. 2011, in ASP Conf. Ser. 448, 16th Cambridge Workshop on Cool Stars, Stellar Systems, and the Sun, ed. C. Johns-Krull, M. K. Browning, & A. A. West (San Francisco, CA: ASP), 91
- Alsubai, K., Mislis, D., Tsvetanov, Z. I., et al. 2017, *AJ*, 153, 200
- Andersen, J., Andersen, M. I., Klougart, J., et al. 1995, *Msngr*, 79, 12
- Artigau, É., Kouach, D., Donati, J.-F., et al. 2014, *Proc. SPIE*, 9147, 914715
- Bakos, G. Á., Csabry, Z., Penev, K., et al. 2013, *PASP*, 125, 154
- Batalha, N. E., Kempton, E. M.-R., & Mbarek, R. 2017, *ApJL*, 836, L5
- Bayliss, D., Gillen, E., Eig Müller, P., et al. 2018, *MNRAS*, 475, 4467
- Bayliss, D., Zhou, G., Penev, K., et al. 2013, *AJ*, 146, 113
- Bakos, G. Á., Torres, G., Pál, A., et al. 2010, *ApJ*, 710, 1724
- Benedict, G. F., Henry, T. J., Franz, O. G., et al. 2016, *AJ*, 152, 141
- Bertin, E., & Arnouts, S. 1996, *A&AS*, 117, 393
- Bovy, J., Rix, H.-W., Green, G. M., Schlafly, E. F., & Finkbeiner, D. P. 2016, *ApJ*, 818, 130
- Brahm, R., Jordán, A., & Espinoza, N. 2017a, *PASP*, 129, 034002
- Brahm, R., Jordán, A., Hartman, J., & Bakos, G. 2017b, *MNRAS*, 467, 971
- Brown, T. M., Baliber, N., Bianco, F. B., et al. 2013, *PASP*, 125, 1031
- Butler, R. P., Marcy, G. W., Williams, E., et al. 1996, *PASP*, 108, 500
- Claret, A. 2018, *A&A*, 618, A20
- Claret, A., Hauschildt, P. H., & Witte, S. 2012, *A&A*, 546, A14
- Claret, A., Hauschildt, P. H., & Witte, S. 2013, *A&A*, 552, A16
- Claudi, R., Benatti, S., Carleo, I., et al. 2018, *Proc. SPIE*, 10702, 107020Z
- Collins, K., & Kielkopf, J. 2013, AstroImageJ: ImageJ for Astronomy, Version 3.2.0, Astrophysics Source Code Library, ascl:1309.001
- Collins, K. A., Kielkopf, J. F., Stassun, K. G., & Hessman, F. V. 2017, *AJ*, 153, 77
- Crane, J. D., Shectman, S. A., & Butler, R. P. 2006, *Proc. SPIE*, 6269, 626931
- Crane, J. D., Shectman, S. A., Butler, R. P., et al. 2010, *Proc. SPIE*, 7735, 773553
- Crane, J. D., Shectman, S. A., Butler, R. P., Thompson, I. B., & Burley, G. S. 2008, *Proc. SPIE*, 7014, 701479
- Cushing, M. C., Vacca, W. D., & Rayner, J. T. 2004, *PASP*, 116, 362
- Cutri, R. M., et al. 2014, *yCat*, 2328, 0
- de Wit, J., & Seager, S. 2013, *Sci*, 342, 1473
- Delfosse, X., Forveille, T., Ségransan, D., et al. 2000, *A&A*, 364, 217
- Dopita, M., Hart, J., McGregor, P., et al. 2007, *Ap&SS*, 310, 255
- Espinoza, N., Bayliss, D., Hartman, J. D., et al. 2016, *AJ*, 152, 108
- Fressin, F., Torres, G., Charbonneau, D., et al. 2013, *ApJ*, 766, 81
- Hansen, B. M. S., & Barman, T. 2007, *ApJ*, 671, 861
- Hartman, J. D., & Bakos, G. Á. 2016, *A&C*, 17, 1
- Hartman, J. D., Bakos, G. Á., Bayliss, D., et al. 2019, *AJ*, 157, 55
- Hartman, J. D., Bayliss, D., Brahm, R., et al. 2015, *AJ*, 149, 166
- Hartman, J. D., Bakos, G. Á., Torres, G., et al. 2009, *ApJ*, 706, 785
- Henden, A. A., Levine, S., Terrell, D., & Welch, D. L. 2015, AAS Meeting, 225, 336.16
- Hippler, S., Bergfors, C., & Brandner, W. 2009, *Msngr*, 137, 14
- Huang, C. X., Burt, J., Vanderburg, A., et al. 2018, *ApJL*, 868, L39
- Jaehrig, K., Somers, G., & Stassun, K. 2019, *ApJ*, 879, 39

- Jenkins, J. M., Twicken, J. D., McCauliff, S., et al. 2016, *Proc. SPIE*, **9913**, 99133E
- Johnson, J. A., Aller, K. M., Howard, A. W., & Crepp, J. R. 2010, *PASP*, **122**, 905
- Johnson, J. A., Gazak, J. Z., Apps, K., et al. 2012, *AJ*, **143**, 111
- Jordán, A., Brahm, R., Bakos, G. Á., et al. 2014, *AJ*, **148**, 29
- Kaufer, A., & Pasquini, L. 1998, *Proc. SPIE*, **3355**, 844
- Kotani, T., Tamura, M., Suto, H., et al. 2014, *Proc. SPIE*, **9147**, 914714
- Kovács, G., Bakos, G., & Noyes, R. W. 2005, *MNRAS*, **356**, 557
- Kovács, G., Zucker, S., & Mazeh, T. 2002, *A&A*, **391**, 369
- Lang, D., Hogg, D. W., Mierle, K., Blanton, M., & Roweis, S. 2010, *AJ*, **139**, 1782
- Latham, D. W., Mazeh, T., Stefanik, R. P., Mayor, M., & Burki, G. 1989, *Natur*, **339**, 38
- Laughlin, G., Bodenheimer, P., & Adams, F. C. 2004, *ApJL*, **612**, L73
- Liu, B., Zhang, X., & Lin, D. N. C. 2016, *ApJ*, **823**, 162
- Madhusudhan, N. 2018, in *Handbook of Exoplanets*, ed. H. Deeg & J. Belmonte (Cham: Springer), 104
- Maíz Apellániz, J., & Weiler, M. 2018, *A&A*, **619**, A180
- Mandel, K., & Agol, E. 2002, *ApJL*, **580**, L171
- Marigo, P., Girardi, L., Bressan, A., et al. 2017, *ApJ*, **835**, 77
- Mordasini, C., Alibert, Y., Benz, W., Klahr, H., & Henning, T. 2012, *A&A*, **541**, A97
- Newton, E. R., Charbonneau, D., Irwin, J., & Mann, A. W. 2015, *ApJ*, **800**, 85
- Obermeier, C., Koppenhoefer, J., Saglia, R. P., et al. 2016, *A&A*, **587**, A49
- Pál, A. 2012, *MNRAS*, **421**, 1825
- Penev, K., Bakos, G. Á., Bayliss, D., et al. 2013, *AJ*, **145**, 5
- Quirrenbach, A., Amado, P. J., Caballero, J. A., et al. 2014, *Proc. SPIE*, **9147**, 91471F
- Rabus, M., Jordán, A., Hartman, J. D., et al. 2016, *AJ*, **152**, 88
- Reiners, A., Zechmeister, M., Caballero, J. A., et al. 2018, *A&A*, **612**, A49
- Ricker, G. R., Winn, J. N., Vanderspek, R., et al. 2015, *JATIS*, **1**, 014003
- Skrutskie, M. F., Cutri, R. M., Stiening, R., et al. 2006, *AJ*, **131**, 1163
- Smith, J. C., Stumpe, M. C., Van Cleve, J. E., et al. 2012, *PASP*, **124**, 1000
- Somers, G., & Stassun, K. G. 2017, *AJ*, **153**, 101
- Southworth, J. 2011, *MNRAS*, **417**, 2166
- Stassun, K. G., Corsaro, E., Pepper, J. A., & Gaudi, B. S. 2018, *AJ*, **155**, 22
- Stumpe, M. C., Smith, J. C., Catanzarite, J. H., et al. 2014, *PASP*, **126**, 100
- Vacca, W. D., Cushing, M. C., & Rayner, J. T. 2004, *PASP*, **116**, 352
- Wheatley, P. J., West, R. G., Goad, M. R., et al. 2018, *MNRAS*, **475**, 4476
- Wildi, F., Blind, N., Reshetov, V., et al. 2017, *Proc. SPIE*, **10400**, 1040018
- Wright, J. T., Mahadevan, S., Hearty, F., et al. 2018, *AAS Meeting*, **231**, 246.45
- Zacharias, N., Finch, C. T., Girard, T. M., et al. 2013, *AJ*, **145**, 44
- Zechmeister, M., & Kürster, M. 2009, *A&A*, **496**, 577
- Ziegler, C., Law, N. M., Baranec, C., et al. 2018, *AJ*, **156**, 259
- Zucker, S., Mazeh, T., Santos, N. C., Udry, S., & Mayor, M. 2003, *A&A*, **404**, 775